optica

Chirped dissipative solitons in driven optical resonators: supplement

CHRISTOPHER SPIESS, QIAN YANG, XUE DONG, VICTOR G. BUCKLEW, AND WILLIAM H. RENNINGER*

Institute of Optics, University of Rochester, Rochester, New York 14627, USA
Corresponding author: william.renninger@rochester.edu

Chirped dissipative solitons in driven optical resonators: supplemental document

1. Numerical methods

Numerical simulations are developed to determine if a cavity consisting of normal dispersion fiber, losses, a drive source, and a spectral filter can support chirped dissipative solitons. The fiber is modeled by a detuned nonlinear Schrödinger equation incorporating dispersive and nonlinear phase modulations in addition to a term corresponding to the frequency detuning of the drive from the peak of the cavity resonance [1]. The fiber section is simulated with the standard split-step Fourier technique with the dispersive effects calculated in the Fourier domain and the nonlinear effects solved with a 4th order Runge-Kutta method. After the fiber section, the loss, drive, and spectral filter are added as lumped elements. The initial cavity under consideration consists of 52.5 m of fiber with $n_2 = 3.2 \times 10^{-20} \frac{m^2}{W}$, β_2 $= 9688 \frac{fs^2}{m}$, and mode-field diameter of d=8.1 μm, total losses of 1.05 dB (as predicted for a typical experimental cavity), and a Gaussian spectral filter with 4-nm spectral bandwidth (and negligible dispersion).

Solutions are identified as stable if the field converges to a steady-state after a finite number of iterations around the cavity (see Supplementary Document, Section 4). For example, the chirped pulse solutions from Fig. 2 are stable, and the mean intensity of the electric field converges to a constant numerically limited value after 500 round-trips, which corresponds to 125 μs for the 50-m cavity with a 4-MHz repetition rate (Fig. 2(a)). The simulations presented have a 100-ps temporal window. The results are unchanged with larger temporal windows. The cavity is seeded by Gaussian or random electric field initial conditions and multiple round trips are simulated. The combination of 9 noisy and 6 Gaussian initial fields results in a sufficient number of stable solutions to establish clear boundaries between different solution types (see Supplementary Document, Section 4).

The chirp is evaluated through the application of anomalous GDD to the pulse, in keeping with the experimental practice of 'dechirping' the pulse with a grating pair dispersive compressor. The chirp magnitude in units of ps² is determined by the GDD required to maximize the pulse peak intensity (Fig. 2(b)). In the example from Fig. 2, with a cavity with a 2-nm spectral filter (intra-cavity drive power 11.4 W and detuning 1.36 rad), the intensity is smoothly maximized and indicates a positive chirp that corresponds to a GDD of 1 ps².

For the dispersion-managed simulations the normal dispersion fiber is modeled as above, the anomalous dispersion fiber is modeled with $n_2 = 3.2 \times 10^{-20} \frac{m^2}{W}$, $\beta_2 = -22946 \frac{fs^2}{m}$, and mode-field diameter of d=10.4 μm, and the third-order dispersion for both fibers is given by β_3 $= 0.1 \times 10^6 \frac{fs^3}{m}$. The spectral filter has a 12th order super-Gaussian response with a full-width at half-maximum bandwidth of 4.25 nm.

To numerically model the resonance as a function of frequency for comparison with experiments we use a noise-seeded simulation in which the detuning is varied after each round trip at a rate determined by the experimental sweep time. The continuous-wave intensity is averaged over 10 different random-intensity initial fields and plotted at each value of detuning (Fig. 3(h)). See Supplementary Document, Section 14 for additional information.

2. Experimental methods

Experimentally, following the results of numerical simulations, a fiber resonator is designed to support chirped dissipative solitons. The cavity consists of a total length of 150-m single-mode fiber with a net-dispersion that corresponds to 52.5-m of normal dispersion fiber (with $\beta_2 = 9688 \frac{fs^2}{m}$). An isolator ensures unidirectional operation and suppresses Brillouin scattering. The drive is coupled into the cavity with a 5% fiber-format coupler, and the output is coupled out from a distinct 2% fiber coupler. A 4.25-nm 12th order super-Gaussian fiber-format spectral filter based on thin film technology is spliced into the cavity after the output coupler. The drive consists of an intensity-modulated narrow-line fiber laser. The intensity-modulator is driven with 10-ns pulses with a 750-ns period matching that of the fiber cavity. The modulated drive is amplified, and residual amplified spontaneous emission is filtered out with a 20-GHz fiber-Bragg grating band-pass filter. 1 W of average power is available before the input fiber coupler and after the filter. Polarization controllers are used to control the polarization state separately before the intensity modulator and before the fiber cavity. The controller before the modulator is varied to optimize the peak power and modulation depth of the drive pulses and the controller before the cavity is aligned such that a single polarization mode is excited in the cavity, which is verified by minimizing the power corresponding to the resonance of the unwanted polarization cavity mode when sweeping the drive frequency through the cavity resonance frequencies as in the swept measurements from Fig. 3(d). The drive frequency is locked to the cavity resonance with a proportional–integral–derivative (PID) control circuit using the 100-mW continuous-wave optical power (derived from the cavity output after a bandpass filter) detected and low-pass filtered as an error signal. The PID circuit enables control of the frequency offset, or detuning, from the cavity resonance. Stable chirped solitons are obtained using a side-lock technique at detuning values near 1 radian blue-detuned from the resonance, in agreement with numerical results (Fig. 1d). While the side-lock technique is effective for demonstrating stable chirped pulses, a Pound-Drever-Hall peak-lock technique may allow for exploration of more detuning values. To measure the cavity resonance, the continuous-wave output power is measured as the laser frequency is swept through the cavity resonance. The laser frequency is periodically swept through the cavity resonance by a piezo-based tuning mechanism driven with a triangle-wave voltage source.

3. Numerical convergence criteria and stability

Numerical convergence criteria are developed to identify novel stable solutions under steady-state conditions. The optical intensity is analyzed to distinguish between trivial continuous-wave solutions, noise states, and the nontrivial solutions of interest. The number of round trips needed for convergence varies from less than 300 to greater than 8000. The cavity is numerically simulated for 2000 round trips, which is enough to reliably distinguish between modes of operation without excessive computation time. The numerical results are identified as continuous-wave solutions first if the difference between the minimum and maximum intensity of the waveform is <0.1 W during the last simulated round trips. Distinguishing between noisy and nontrivial converged solutions is more involved. For this analysis we examine the maximum value of the intensity during the last 100 round trips simulated. Two types of convergence are found: convergence to a constant maximum intensity value and convergence to an intensity value that varies over a constant integer (>1) number of round trips. The constant convergence case can be identified by solutions with minimal variation of the maximum intensity over the last 100 round trips and the periodically converging solutions are identified through a Fourier analysis of the intensity over the last 100 round trips. After the solutions are analyzed for convergence, the continuous-wave solutions and noisy non-

converged solutions are identified by white space, and the converged solutions are identified by a color associated with a pulse parameter of interest (e.g. number of peaks in Fig. 1(b) and other metrics in Supplementary Document, Section 5). For a given set of system parameters, multiple solutions are possible, which can result in multiple types of convergence. Therefore, the type of convergence is a function of the simulated initial conditions.
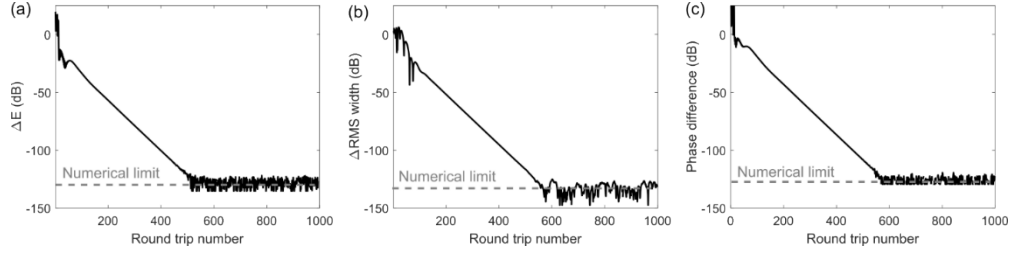

Fig. S1. Convergence and stability of chirped pulses. The difference in the (a) total energy, (b) root-mean-squared pulse width, and (c) temporal phase integrated over the central 2 ps of the pulse of the simulated electric field between subsequent round trips.

Chirped pulse solitons rapidly converge to their steady state in the cavity after a few hundred round trips. The convergence of the difference in energy after subsequent round trips, as shown in Fig. 2(a) of the manuscript, is a simple and reliable indicator of stability for chirped solitons. Here we show that in addition to pulse energy, the full complex electric field converges and is also stable for chirped dissipative Kerr resonator solitons. With the same steady-state cavity parameters as in Fig. 2, and a unique initial condition, stable chirped pulses are obtained, and the convergence is evaluated in Fig. S1. The energy difference converges to a numerical limit after around 500 roundtrips (Fig. S1(a)). In addition, the RMS temporal pulse duration converges to a numerically limited value after around 600 roundtrips (Fig. S1(b)). Finally, the temporal phase convergence is evaluated using the difference integral in temporal phase over 2 ps centered at the peak of the ~8-ps pulse between subsequent cavity round trips. Changes in the temporal phase also rapidly converge to a numerically limited value after around 600 round trips. The convergence of the full complex electric field indicates that chirped dissipative solitons are strictly stable in numerical simulations.

4. Numerical dependence on initial conditions

The steady-state solutions of the driven-cavity system are strongly sensitive to the initial waveform used to seed the numerical simulations. Moreover, it is challenging to find the appropriate initial conditions for obtaining non-trivial steady-state solutions. Even when a stable non-trivial solution exists with a particular set of system parameters, many initial waveforms result in the trivial continuous-wave solution, which is often also stable. For example, Fig. S2(b) represents all the converged non-trivial solutions obtained from a single Gaussian initial waveform with a width of 3 ps and 10-W peak power. The colored region is much sparser because many of the parameters where non-trivial solutions were previously identified (Fig. S2(a)) now converge to the trivial continuous-wave solution instead. In this case the chirped pulses are not observed at all. If instead, a completely random white-noise initial condition is used (where each point in time corresponds to a power that varies from 0 W to a maximum power of 143 W), a different subset of nontrivial solutions is revealed (Fig. S2(c)), including several of the chirped pulses. Notice that neither initial conditions result in all of the non-trivial solutions. In these examples, the chirped pulses only appear with the noisy initial condition and the solutions near 2.5 rad only appear with the Gaussian initial condition.
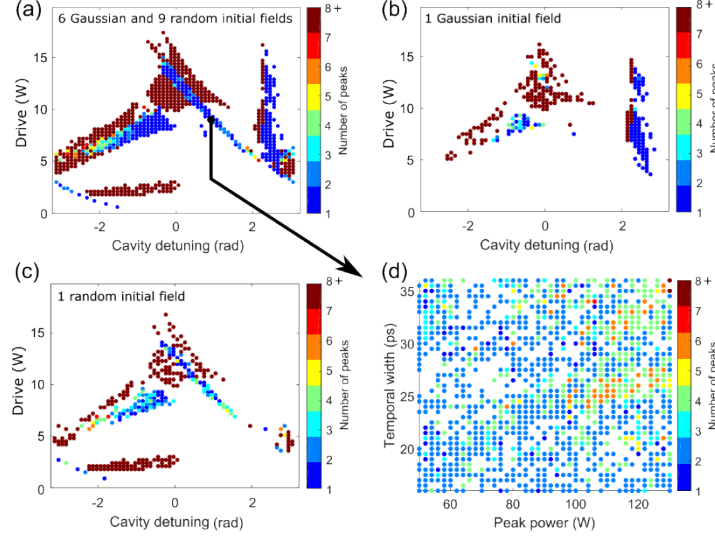
Fig. S2. Numerical sensitivity to initial conditions. (a) Converged solutions from Fig. 1(b) including the results from 15 different initial fields, with 9 random profiles and 6 different Gaussian profiles. The minimum number of peaks among the converged solutions is plotted for each pair of drive power and detuning values. (b) Converged solutions given a single Gaussian initial filed with 10-W peak power and 3-ps pulse width. (c) Converged solutions given a single initial condition with random intensity variations. (d) Illustration of different converged solutions as a function of the duration and peak power of the input Gaussian field for the drive frequency and detuning indicated from (a). White space represents continuous-wave or non-converged solutions.

To evaluate the dependence on initial conditions in more detail, for a single set of system parameters, we examine the converged solutions for many different Gaussian initial fields parametrized by temporal width and peak power (Fig. S2(d)). We find a complex arrangement of solutions as a function of these initial conditions. In Fig. S2(d), the white regions indicate the continuous-wave solution and the color represents the number of nontrivial pulses in the converged waveform. There is considerable variation in the character of the converged solutions for small changes in the initial condition. Therefore, to maximize the probability of obtaining nontrivial solutions, for each choice of system parameters we examine many initial conditions and retain only the nontrivial solutions. Specifically, we find a good optimization of solutions obtained vs. computation time with 15 initial conditions, including 9 random initial fields (where the power varies from 0 to 143 W) and 6 Gaussian initial fields (with 10-W peak power and a pulse width that varies in equally spaced increments from 500 fs to 3 ps). This set of initial conditions was used to obtain the solutions illustrated in Fig. S2(a), for example. Owing to this sensitive dependence on initial conditions, it is likely that the results presented are incomplete and that with alternative initial conditions stable solutions could be obtained for additional parameters.

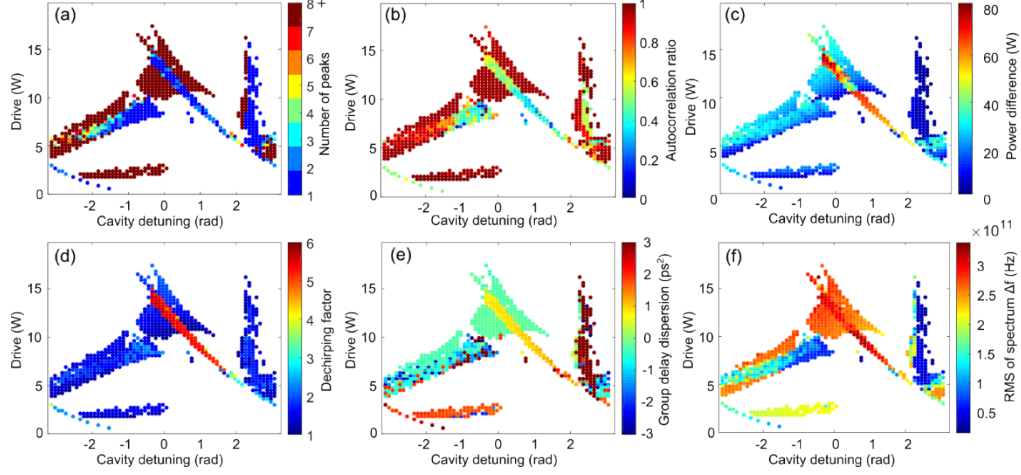## 5. Evaluating and distinguishing stable numerical solutions

Fig. S3. Evaluating different parameters of the steady-state solutions. Converged solutions as a function of drive power and detuning for an all-normal dispersion cavity. The color maps represent (a) the number of prominent intensity peaks, (b) the intensity periodicity defined by the ratio of the central peak to the neighboring peak of the autocorrelation of the intensity profile (1 corresponds to a highly periodic pattern), (c) the difference between the maximum and minimum of the waveform power in the time domain, (d) the ratio of the peak power after external compression to that before, e the group delay dispersion required to maximize the ratio in (e), and (f) the root-mean-squared bandwidth of the output spectrum.

The results of the numerical simulations are illustrated as a function of two experimentally convenient variables, the drive power and the detuning. In Fig. S3(a) (and Fig. 1 of the paper), the number of intensity peaks is indicated by a color for each converged solution as a function of drive power (y-axis) and detuning (x-axis). In this case, the minimum number of peaks observed from among the converged solutions seeded by 15 different initial conditions (see the previous Section) is represented in the plot. The number of intensity peaks is a useful solution parameter because it resolves different classes of solutions in parameter-space particularly well. However, other waveform parameters provide valuable and complementary information. Here we examine multiple parameters of the complex stable solutions observed in normal dispersion driven cavities with spectral filtering. The periodicity of the waveforms can be defined by the contrast ratio between the central intensity and neighboring points of a numerical autocorrelation of the waveform in time. If this ratio is one, the solution is periodic and if this ratio is zero, the solution is aperiodic. In this case, the lowest ratio from among the converged solutions seeded by 15 different initial conditions is represented in Fig. S3(b). The periodicity highlights periodic Turing waves (red in Fig. S3(b)) as well as single pulses, such as the chirped-pulses (light-green region in Fig. S3(b)). While related, this information is distinct from the total number of prominent peaks (compare Fig. S3(a) and Fig. S3(b)). Because the chirped-pulse, dark soliton, and switching wave solutions each have a small number of peaks the contrast between these solutions and the Turing patterns is slightly larger for this parameter (e.g. dark blue regions of Fig. S3(a)). The chirped-pulse peak power is large even before dechirping, which is evident when examining the difference between the waveform maximum and minimum powers (Fig. S3(c)). To clearly distinguish the chirped pulses from other solutions we examine the ratio of the waveform peak power after dechirping to its peak power

before dechirping and represent in Fig. S3(d) the maximum of this ratio from among the converged solutions obtained from all 15 initial conditions. The waveforms are dechirped by applying anomalous group-delay dispersion until the peak power is maximized. The corresponding magnitude of this dispersion is also plotted in Fig. S3(e). However, while this is useful information for a waveform with a dechirping factor >2, as it is for chirped pulses, it is less useful for waveforms that do not change in peak intensity with the application of dispersion, because this implies that the pulses do not have significant or well-defined quadradic spectral phase. Finally, the spectral bandwidth (the maximum rms bandwidth from among all the converged solutions obtained from 15 initial conditions is plotted in Fig. S3(f)) is of interest for applications. Notably, the solutions with the largest spectral bandwidth include the chirped pulses (red) and the Turing patterns (orange). Overall, the chirped pulses are characterized by few peaks, low periodicity, a high-power difference, large dechirping factor that corresponds to 1 ps^2 of GDD, and broad bandwidth. Chirped dissipative solitons can be distinguished through most of these parameters, as illustrated in Fig. S3.

6. Coexisting nonlinear solutions

Driven fiber optical cavities are complex nonlinear systems that can support a variety of stable structures. In cavities with anomalous dispersion, two commonly observed solutions are solitons and Turing patterns. Notably, these distinct nonlinear solutions have also been found to coexist, with a single soliton stabilized on a stable Turing pattern [2]. This type of nonlinear coexistence is also found in several variations in the normal dispersion system with a spectral filter examined here. In the normal dispersion system, Turing patterns are stable over large regions of parameter space (Fig. S4 red), with a particularly large region of stable solutions between 10 and 15 W of intra-cavity drive power. The chirped pulses, as discussed previously, are stable over a large region between 5 and 15 W of drive power (Fig. S4 blue line). Noticeably, these two regions overlap between 10 and 15 W. In the overlapping region the two nonlinear solutions coexist, and the chirped pulses exist on top of a periodic background. The chirped pulses therefore exhibit a continuous-wave background for drive powers smaller than 10 W and an oscillating background for greater powers (Fig. S4). In addition to the Turing and chirped-pulse coexistence we also find coexistence between many other combinations of the observed stable nonlinear waveforms. One immediate consequence of this complicated coexistence behavior is the resultant difficulty in interpreting the solution parameters introduced in Supplementary Section 3.
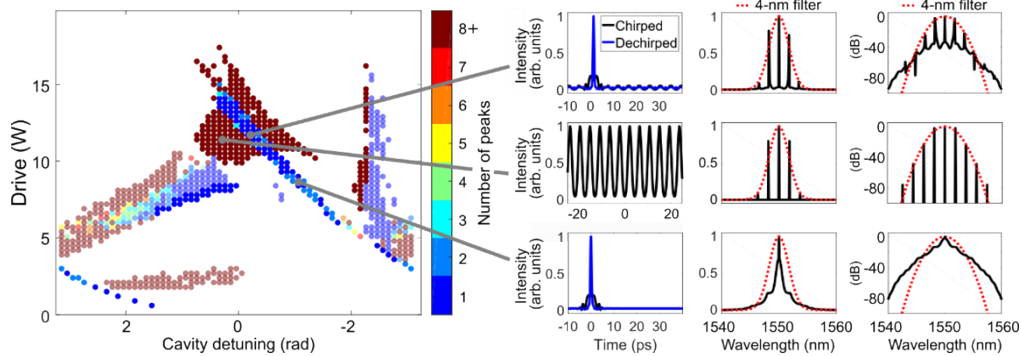

Fig. S4. Coexistence of nonlinear solutions. The chirped pulses (blue region in the plot on the left and bottom row on the right) and the Turing patterns (red regions in the plot on the left and

middle row on the right) coexist in parameter space resulting in a nonlinear solution combining the two solutions (top row on the right). The corresponding temporal intensity and the spectral intensity in linear and log scales are represented on the right with the dechirped pulse plotted with a blue line and the 4-nm spectral filter plotted with a red dashed line.

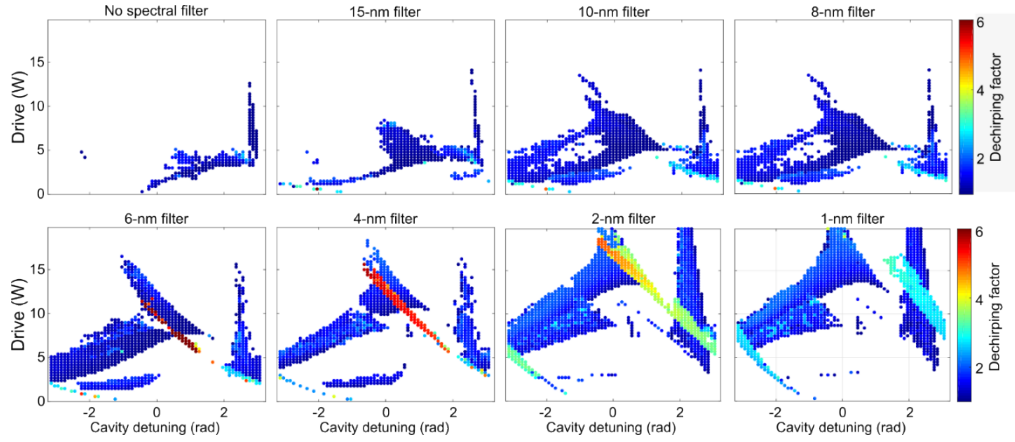## 7. Dependence on the filter bandwidth

Fig. S5. Chirped dissipative soliton existence vs. spectral filter bandwidth. The dechirping factor for converged solutions vs. intra-cavity drive power and detuning for different bandwidths, $\Delta\lambda$ (full width at half the maximum), of a Gaussian spectral filter for a cavity length of 52.5 m. Stable chirped pulses appear for filter bandwidths less than 8 nm. Higher compression factors are observed with broader filter bandwidths (red).

The filter bandwidth must be chosen appropriately to stabilize chirped pulses in the cavity. To evaluate the dependence of the regions of existence on the spectral filter bandwidth, numerical simulations are performed with the same parameters as the all-normal dispersion cavity (52.5 m length, Gaussian filter), but with varying filter bandwidths. Changes to the stable chirped pulses over a range of drive powers and detuning values can be identified with the dechirping factor (Fig. S5). Chirped pulses are not observed without a spectral filter in the cavity. Chirped pulses begin to appear for Gaussian filters with full-width at half maximum bandwidths of 8 nm or narrower. Full width at half maximum bandwidths between 6 and 4 nm enable chirped pulses with high dechirping factors over a broad range of detuning values. This range therefore defines the optimum filter bandwidths for this cavity. The threshold for chirped pulses is approximately 5 W with a 6-nm filter bandwidth. With smaller drive powers, switching waves are observed instead. The threshold decreases with narrower spectral filter bandwidths. For example, the threshold is 2.5 W with a 2-nm filter, where the switching waves obtained with the broader filter become chirped pulses. Narrower filter bandwidths reduce the threshold further but with a corresponding decrease in the bandwidth and the chirped-pulse compression ratio. From Eq. 1, the stability regions obtained for a given filter (e.g. 6 nm) can be recovered with a different filter bandwidth (e.g. 8 nm) by making a corresponding change in the total group delay dispersion (e.g. with $(6/8)^2$ times less dispersion).

8. Chirped cavity soliton dynamics

The dynamics of the chirped dissipative solitons depend on the parameters of the cavity. Fig. 2 of the paper depicts the evolution of chirped solitons from an all-normal dispersion cavity with a 2-nm Gaussian spectral filter, an intra-cavity drive power of 11.4 W, and a detuning of 1.36 rad. This configuration yields one of the least complex evolution dynamics among the chirped-pulses solutions observed. In this section, we describe examples of more complex dynamics observed for chirped-pulse solutions with different parameters. While the essential characteristics are the same including the consistently large positive chirp and broad spectral bandwidth, the details of the evolution such as the pulse compression factor and the solution periodicity, can vary.
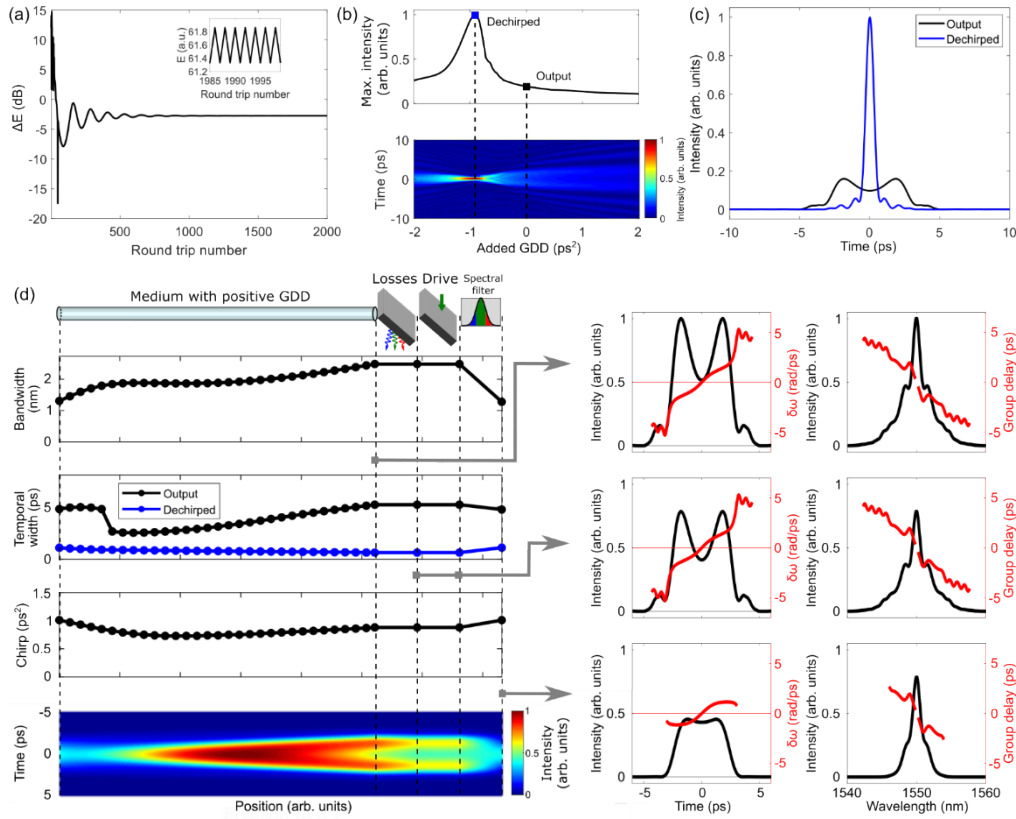

Fig. S6. Characteristics of chirped dissipative solitons with a broader, 4-nm filter. (a) Numerical convergence of the pulse energy difference between subsequent round trips, ΔE, to a stable numerically-limited steady-state value. The pulse energy of the last 15 round trips is plotted inset to depict the period-2 oscillation. (b) The change in the pulse and peak intensity as a function of group-delay dispersion applied after the cavity, indicating compression with anomalous dispersion with a maximum at GDD = -0.9 ps^2. (c) The chirped cavity output (black) and dechirped (blue) pulses from (b). (d) Evolution of steady-state chirped dissipative soliton bandwidth (FWHM), temporal width (FWHM), chirp (defined by the GDD required to maximize the pulse intensity, with the opposite sign), and pulse intensity in the cavity. The FWHM of the pulse after dechirping the pulse at each position of the cavity is plotted in blue. The associated pulse intensity, instantaneous frequency, power spectrum, and group delay from the indicated locations in the cavity are plotted on the right.

Broader filter bandwidth. The filter bandwidth is a critical parameter in determining the character of the solutions. For comparison with the results of a 2-nm spectral filter (Fig. 2), we examine a solution with a 4-nm spectral filter (Fig. S6). This solution exists with 9.6-W intra-cavity drive power and 0.62-rad detuning. An interesting difference with this solution can be seen in the convergence (Fig. S6(a)). The solution converges to a periodic solution alternating between slightly different peak powers (<1% variation) every other round trip. While qualitatively distinct, this small change has a negligible effect on the pulse dynamics. Interestingly, for this filter bandwidth only solutions with this 2-period convergence are observed (after 2000 round trips). The chirp is similar to the previous case which corresponds to a GDD of approximately 0.9 ps^2 with a dechirping factor of ~6 (Fig. S6(b)-(c)). The broader bandwidth associated with the broader filter results in a shorter compressed pulse with a duration of 600 fs. The qualitative evolution of the spectrum is the same, with a bandwidth increase in the waveguide due to nonlinear broadening and a decrease from the spectral filter (Fig. S6(d)). The temporal pulse duration evolution is also qualitatively similar with an overall increase due to dispersion but with a steeper drop of the pulse duration in the first fiber section. Overall the chirped pulses observed with different filter bandwidths are qualitatively similar but with small quantitative differences. In this case the broader filter bandwidth supports a chirped dissipative soliton with a broader bandwidth.
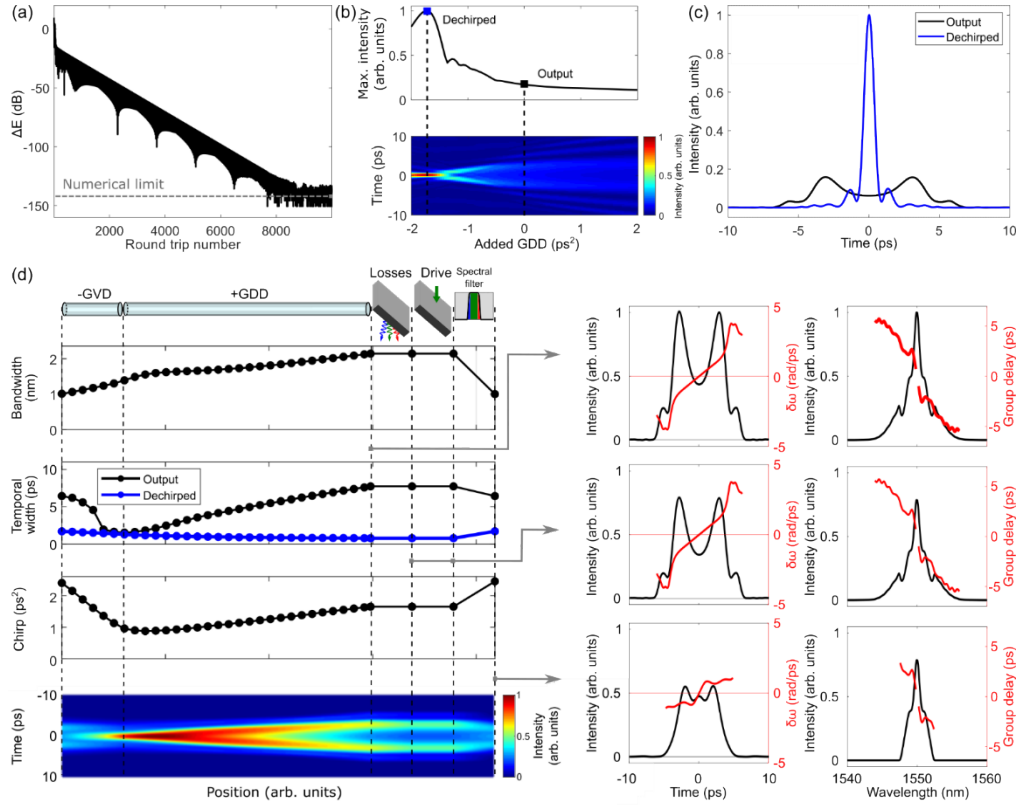

Fig. S7. Characteristics of chirped dissipative solitons from Region i in the net-normal dispersion cavity. (a) Numerical convergence of the pulse energy difference between subsequent round trips, ΔE, to a stable numerically-limited steady-state value. (b) The change in the pulse and peak intensity as a function of group-delay dispersion applied after the cavity, indicating compression with anomalous dispersion with a maximum at GDD = -1.7 ps^2. (c) The chirped cavity output (black) and dechirped (blue) pulses from (b). (d) Evolution of steady-

state chirped dissipative soliton bandwidth (FWHM), temporal width (FWHM), chirp (defined by the GDD required to maximize the pulse intensity, with the opposite sign), and pulse intensity in the cavity. The FWHM of the pulse after dechirping the pulse at each position of the cavity is plotted in blue. The associated pulse intensity, instantaneous frequency, power spectrum, and group delay from the indicated locations in the cavity are plotted on the right.

Chirped pulses in a net-normal dispersion cavity. As described in the paper, a longer cavity is beneficial for reducing the drive power threshold and increasing the peak power of the pulsed drive source. A 150-m cavity was designed with a net-normal dispersion equivalent to that of the shorter 52.5-m cavity. This was achieved through introducing anomalous dispersion fiber   Additionally, motivated by the experimental parameters the filter is implemented as a 12th order super-Gaussian spectral filter with a FWHM bandwidth of 4.25 nm and the round-trip loss is 1.05 dB. The solutions from this cavity are represented in Fig. 1(d) for comparison with the all-normal dispersion case (Fig. 1(b)) in the main paper. The additional fiber sections may also impact the evolution of the chirped pulses in the cavity. We examine these differences for the chirped pulses from Regions i and ii from Fig. 1(d).

Region i. Fig. S7 depicts pulses with an intra-cavity drive power of 2.95 W and a detuning of 0.9 rad in chirped-pulse Region i. This solution requires 8000 round trips to reach numerically-limited convergence (Fig. S7(a)) and the dechirping factor remains similar, with a value of ~6 (Fig. S7(b)-(c)). The spectral bandwidth increases in both of the waveguide sections through nonlinear broadening and then decreases with the application of the filter. The pulse duration now decreases in the anomalous dispersion fiber as the pulse is partially dechirped (Fig. S7(d)). The residual pulse broadening is compensated by a reduction through spectral filtering. The chirp is larger than in the all-normal dispersion cavity, and corresponds to a GDD of 1.7 ps^2 on the pulse output before the spectral filter. This is in part because of the additional normal dispersion fiber that is required to form the additional dispersion map. The pulse (with two peaks) and the spectrum look qualitatively similar to those in the all-normal dispersion case. Overall, this solution is very similar to that from the all-normal dispersion cavity with small changes originating from the additional segments of fiber.

Region ii. Fig. S8 depicts pulses with an intra-cavity drive power of 3.8 W and a detuning of 0.43 rad in chirped-pulse Region ii. In this case the solution requires two round trips before the evolution repeats. Unlike in Fig. S6 where the pulse varies by <1% between round trips, in this case the variation is >10% (Fig. S8(a)). In Fig. S8(b)-(c) and Fig. 3 of the paper, the average of the dechirped pulse from each round trip is plotted. The averaged dechirping factor is slightly smaller than with a peak power increase of ~4 after dechirping. The large variation of peak power every round trip requires evaluating the pulse evolution over two subsequent round trips in Fig. S8(d). While subtle differences can be identified, the overall evolution remains qualitatively the same: the spectral bandwidth and pulse duration have a net increase in the fiber sections and are both decreased back to their initial values after spectral filtering. The chirp from pulses in Region ii is large throughout the evolution, with an output chirp of 1.4 ps^2. Experimentally, the average between the output waveforms from each of the two round trips is measured. While the simulated chirped-pulse solutions are all qualitatively similar, the solutions from Region ii have the closest quantitative agreement with the chirped pulses observed experimentally.
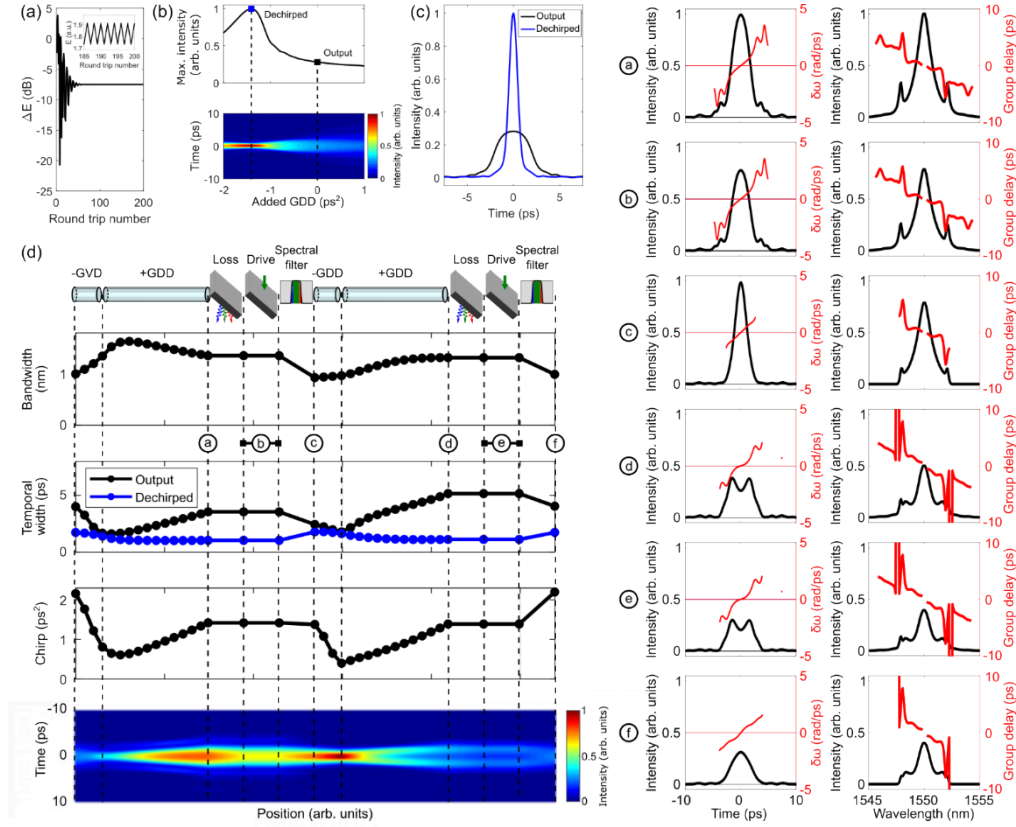
Fig. S8. Characteristics of chirped dissipative solitons from Region ii in the net-normal dispersion cavity. (a) Numerical convergence of the pulse energy difference between subsequent round trips, ΔE, to a stable numerically-limited steady-state value. The pulse energy of the last 15 round trips is plotted inset to depict the period-2 oscillation. (b) The change in the pulse and peak intensity as a function of group-delay dispersion applied after the cavity, indicating compression with anomalous dispersion with a maximum at GDD = -1.4 ps^2. (c) The chirped cavity output (black) and dechirped (blue) pulses from (b). (d) Evolution of steady-state chirped dissipative soliton bandwidth (full width at half the maximum, FWHM), temporal width (FWHM), chirp (defined by the GDD required to maximize the pulse intensity, with the opposite sign), and pulse intensity in the two last round trips of the cavity. The FWHM of the pulse after dechirping the pulse at each position of the cavity is plotted in blue. The associated pulse intensity, instantaneous frequency, power spectrum, and group delay from the indicated locations in the cavity are plotted on the right.

9.   Relative contributions of physical effects

It can be challenging to develop an intuitive or physical explanation for the solutions to complex nonlinear solutions such as the chirped solitons presented. However, a couple of distinctions in the balance of pulse forming mechanisms can be emphasized between the chirped and traditional solitons.   The phase and amplitude balance of nonlinearity, dispersion, and the filter in the time and frequency domains is described qualitatively in Fig. S9.   For the traditional soliton in the anomalous dispersion regime in both the time and frequency domains

the nonlinearity and dispersion produce pure phase modulations, which exactly balance. However, for the chirped soliton in the normal dispersion regime, the amplitude of the pulse and spectrum is also affected, resulting in a more complex and intricate balance. The phase modulation from normal dispersion applied to a chirped pulse cancels out with the phase modulation from nonlinearity in both the time and frequency domains. The amplitude balance in both domains can be understood as follows: the pulse gets longer in time in the fiber section due to dispersion, and the spectrum grows in bandwidth in the fiber section due to nonlinearity. The spectral filter directly reduces this bandwidth growth for balance in the spectral domain. Finally, because the pulse is chirped, a reduction in bandwidth also corresponds to a reduction in pulse duration because the lowest and highest frequencies are in the wings of the pulse. This reduction in duration compensates for the increase from the dispersion in the fiber, resulting in a complete balance of all of the major effects. From this picture it is clear that without the filter the changes in amplitude in the time and frequency domain could not be counter-acted and no bright pulse solution is possible. Beyond this, the drive power has some influence on these dynamics which will modify this picture slightly. A comprehensive study of this intricate dissipative balance may be valuable for future study.
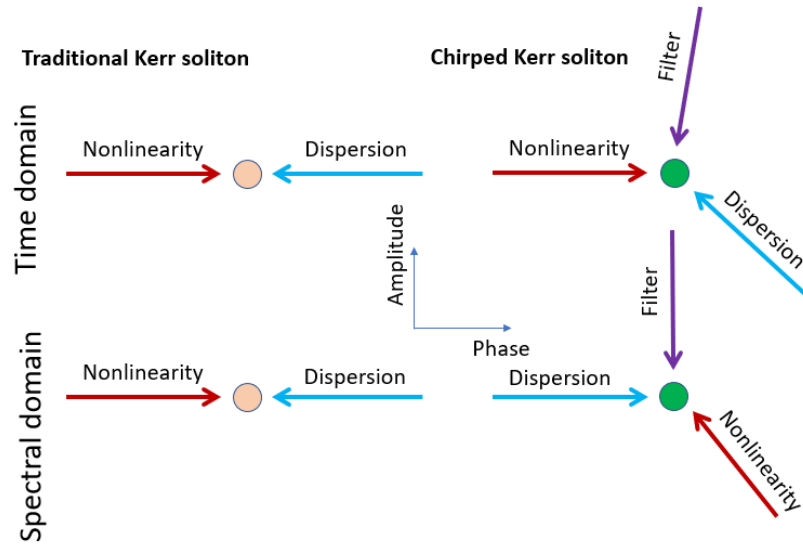

Fig. S9. Relative contributions of the time dependent pulse shaping mechanisms for the traditional and chirped Kerr solitons in amplitude and phase.

10. Dissipation per round trip

Chirped dissipative solitons are stable despite experiencing large levels of dissipation upon traversing the cavity. The dissipation in the cavity stems from the spectral filter in addition to several optical components that result in broadband loss. The spectral filter provides a frequency selective loss that reduces the spectral intensity at either end of the spectrum. Broadband loss results from optical components including the couplers, the isolator, and additional fiber loss. These losses are accounted for in numerical simulations as a lumped dissipative element at the end of each round trip. The overall effect of the dissipative elements can be visualized in the spectral domain (Fig. S10). The corresponding numerical value for the

dissipation is determined by calculating the pulse energy as the product of the peak pulse intensity with the full-width at half maximum duration of the pulse.
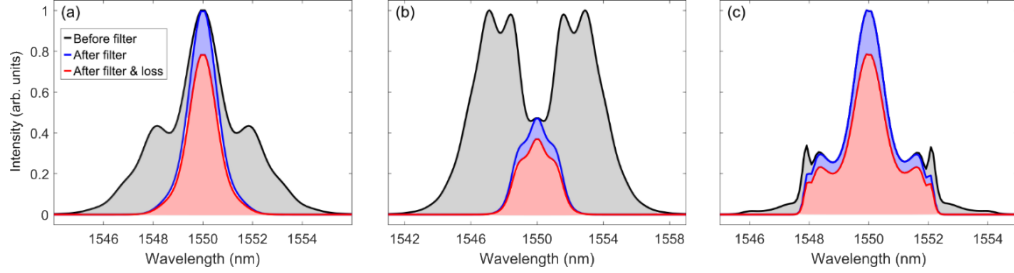

Fig. S10. Spectra of chirped dissipative solitons depicting the effects of dissipation from the spectral filter in addition to other broadband sources of dissipation. (a) Chirped dissipative soliton from Fig. 2 for the main paper, in a cavity with a 2-nm Gaussian filter. This solution features a total dissipation per round trip of 69.5%. (b) In the same cavity, a solution is stable despite a total loss per round trip of 92.1%. (c) The solution corresponding to the results in Fig. 3 in the main paper (and Fig. S8) with a 4.25 super-Gaussian spectral filter. In this case the total dissipation per round trip is 35.8%.

We examine three specific cases to illustrate the stability of chirped dissipative solitons for a variety of dissipation levels. For a typical example, we examine the solutions highlighted in detail in Fig. 2 of the main paper (Fig. S10(a)). In this case a 2-nm Gaussian spectral filter noticeably reduces the magnitude of the spectral side lobes, and the additional frequency independent losses further reduce the spectral power. The resulting total loss during one round trip for this solution is 69.5%. For the same cavity, solutions are stable with higher dissipation (Fig. S10(b)). In this case, the dissipation dynamics are complicated by the fact that the solution is periodic after two full round trips. In one round trip, the spectrum experiences very large relative spectral filtering, resulting in a total loss of 92.1%. This incredible loss arises despite the same 2-nm spectral filter because in this case a large fraction of the energy is in the side lobes of the spectrum before filtering. A third case represents the numerical solution that most closely represents the experimental results presented in Fig. 3 of the main paper (Fig. S10(c)). Here the filter has a super-Gaussian profile with a broader 4.25-nm bandwidth, resulting in a total dissipation in one round trip of 35.8%. Dissipation is essential for chirped dissipative soliton pulse formation since spectral filtering is required. This is in contrast with traditional solitons in anomalous dispersion cavities where stable solutions can form even with zero dissipation [3]. This new dissipative environment may enable opportunities for exploring new strongly dissipative behavior including soliton explosions [4] and dissipative soliton resonances [5].

11. Chirped-pulse scaling laws

Simple scaling laws relating solution parameters to the system parameters can be derived from a master equation model of the cavity. The damped and detuned driven nonlinear Schrödinger equation, or the Lugiato-Lefever equation (LLE), is an established model for the driven nonlinear optical cavity without a filter. The spectral filter essential for chirped pulse generation is modeled with an additional term with a second derivative with respect to time, which corresponds to a Gaussian spectral filter. The LLE with a spectral filter for a slowly varying electric field envelope A is given as

$$L\frac{\partial A}{\partial z} = -\alpha A + i\delta A + \left(i\frac{\overline{\beta_2}}{2}L + \frac{1}{f^2}\right)\frac{\partial^2 A}{\partial t^2} + i\gamma L|A|^2 A + \sqrt{D} \tag{1}$$

where z is the propagation coordinate, t is the fast time, L is the length of the cavity, α corresponds to the cavity loss, δ is the round-trip detuning, $\overline{\beta_2}$ is the average group-velocity dispersion (GDD divided by L), γ is the Kerr nonlinear parameter, f is the spectral filter bandwidth, and D is the intra-cavity drive power. Note that the loss is assumed to be independent of length, as in the experimental cavity in which loss primarily originates from local fiber components. By normalizing z, t, and A in the following way,

$$z' = \frac{z}{z_{n0}} = \frac{z}{L}, \qquad \tau = \frac{t}{T_{n0}} = t\sqrt{\frac{\alpha}{L|\overline{\beta_2}|}}, \quad \text{and} \quad u = A\sqrt{\frac{1}{P_{n0}}} = A\sqrt{\frac{\gamma L}{\alpha}}, \tag{2}$$

Eq. 1 can be rewritten as

$$\frac{1}{\alpha}\frac{\partial u}{\partial z'} = -u + i\frac{\delta}{\alpha}u + \left(i\frac{\text{sgn}(\overline{\beta_2})}{2} + \frac{1}{L|\overline{\beta_2}|f^2}\right)\frac{\partial^2 u}{\partial \tau^2} + i|u|^2 u + \sqrt{\frac{D\gamma L}{\alpha^3}}. \tag{3}$$

By equating the left-hand side to zero to account for steady-state conditions, Eq. 3 becomes

$$0 = -u + i\frac{\delta}{\alpha}u + \left(i\frac{\text{sgn}(\overline{\beta_2})}{2} + \frac{1}{L|\overline{\beta_2}|f^2}\right)\frac{\partial^2 u}{\partial \tau^2} + i|u|^2 u + \sqrt{\frac{D\gamma L}{\alpha^3}}. \tag{4}$$

The resultant normalized equation,

$$0 = -u + i\delta_{n0}u + \left(\frac{i}{2} + \frac{1}{f_{n0}^2}\right)\frac{\partial^2 u}{\partial \tau^2} + i|u|^2 u + \sqrt{D_{n0}}, \tag{5}$$

is defined in terms of three unitless parameters corresponding to the normalized drive (D_{n0}), spectral filter (f_{n0}), and detuning (δ_{n0}) coefficient, given by

$$D_{n0} = D\frac{\gamma L}{\alpha^3}, \quad f_{n0} = f\sqrt{L|\overline{\beta_2}|}, \quad \text{and} \quad \delta_{n0} = \frac{\delta}{\alpha}. \tag{6}$$

If chirped dissipative solitons are known to be stable in a cavity with specific values of D_{n0}, f_{n0} and δ_{n0}, stable chirped solitons can be obtained for a different cavity if the values for the unitless coefficients do not change. The first relationship from Eq. 6 reveals that the required drive power has a cubic dependence on the total cavity loss and an inverse linear dependence on the total cavity nonlinearity (see Supplementary Document, Section 12). The second relationship conveys that the filter bandwidth must scale inversely with the square root of the total group delay dispersion (see Supplementary Document, Section 7). The third relationship suggests that the same solution can be recovered if the relative drive frequency scales linearly with the cavity loss.

The peak power, pulse duration, and energy also scale according to the system parameters, as defined by Eq. 2:

$$T_{n0} = \sqrt{\frac{L|\overline{\beta_2}|}{\alpha}}, \quad P_{n0} = \frac{\alpha}{\gamma L}, \quad \text{and} \quad E = T_{n0}P_{n0} = \frac{\alpha}{\gamma L}\sqrt{\frac{L|\overline{\beta_2}|}{\alpha}} = \frac{1}{\gamma}\sqrt{\frac{\alpha|\overline{\beta_2}|}{L}}. \tag{7}$$

Eq. 7 reveals that broader bandwidths can be achieved with smaller dispersion and that large pulse energies are achieved with smaller nonlinearity and larger dispersion. The scaling laws from Eq. 6 enable efficient design of cavities that can support experimentally realizable chirped dissipative solitons. They can be readily applied to very different parameter regimes and platforms, including for micro-scale comb generation on-chip, or for macroscopic enhancement cavities.
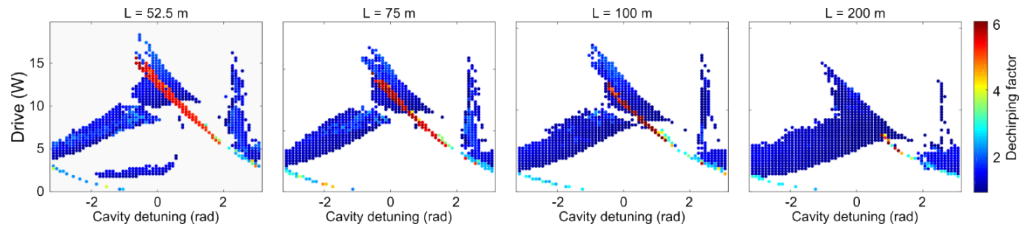
12. Dependence on the cavity length

Fig. S11. Chirped dissipative soliton existence vs. cavity length. Illustration of the dechirping factor for converged solutions vs intra-cavity drive power and detuning for different cavity lengths, L, with a constant 4-nm spectral filter. Increasing the cavity length has a similar effect to increasing the spectral filter bandwidth: stable chirped pulses become sparser in parameter-space.

The length of the cavity determines the total nonlinearity and the group-delay dispersion. From Eq. 6, changes to the total nonlinearity change the drive power threshold and changes to the group-delay dispersion change the required filter bandwidth. To examine and verify these effects, we examine the dependence of the regions of existence on the cavity length with numerical simulations, with all other parameters held constant (Fig. S11). The upper intra-cavity drive power limit varies from 15 W to 10 W for a cavity that is 50% longer, in agreement with the predicated linear relationship. As the length of the cavity is increased further, the number of parameter values where chirped pulse solutions exist decreases dramatically. This can be understood from the relation between the filter bandwidth and the cavity length in Eq. 6. From Fig. S5 and Supplementary Document Section 7, we found that chirped pulses are not observed when the filter is too large. In other words, when the normalized filter bandwidth, f_{n0}, is too large, stable solutions do not exist. From Eq. 6, increasing the cavity length also increases f_{n0} and so we would also not expect to find stable chirped pulse when the cavity is too long. However, this relation also reveals that for long cavities, a value of f_{n0} that supports stable chirped solitons can be recovered with a spectral filter with a narrower bandwidth. Simulations of the dependence of the solutions on length and on spectral filter bandwidth confirm the validity Eq. 6.
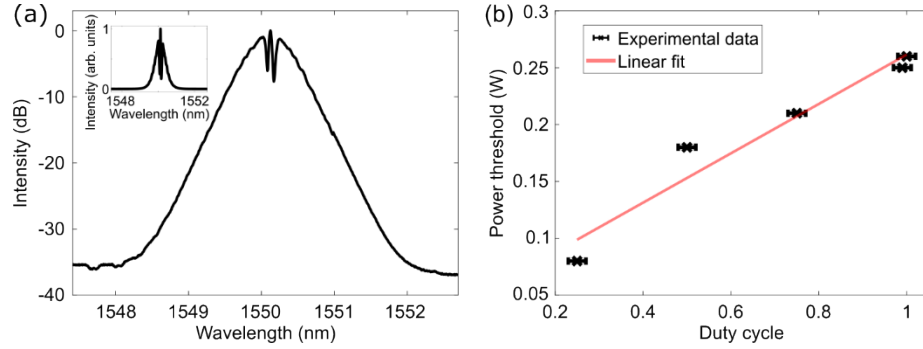
13. Driving the cavity with pulses

Fig. S12. A pulsed drive source enables higher drive powers. (a) Output spectrum on a log scale of experimentally observed anomalous dispersion solitons, with the linear scale inset. (b) Minimum average power of the amplifier required for observing stable solitons vs. the duty cycle of the drive, illustrating a linear increase of the drive peak power.

High drive powers are required to observe stable chirped dissipative solitons. The required high drive powers can be achieved by modulating the continuous wave drive into nanosecond pulses before amplification. The effective drive power is then enhanced by the ratio of the drive pulse duration to the cavity period, which enable two orders of magnitude enhancement for the parameters used in this study. To confirm that the drive power enhancement scales as expected, pulse pumping is applied to a cavity which produces traditional solitons in the anomalous dispersion regime (Fig. S12(a)). The continuous-wave drive power threshold for a 107-m long anomalous dispersion cavity is approximately 0.25 W of average power. By decreasing the duty cycle of the drive, the amplified peak power increases which should enable a corresponding decrease in the average power required by the amplifier. The required average power requirement decreases as expected (Fig. S12(b)), which validates the pulsed drive approach experimentally.

14. Simulation and measurements of the nonlinear cavity resonance

The cavity resonance contains a large amount of global information about the complex nonlinear system. In the paper, a single resonance from experiment is examined and compared to an equivalent numerical simulation, with good qualitative agreement. The goal of this section is to provide more information about this complex resonance, including additional experimental data and corresponding numerical results. Experimentally, the resonance is obtained from the time-integrated cavity output intensity as a function of the drive frequency when swept through the cavity resonance. The data from Fig. 3 corresponds to a drive amplifier power of 1.8 W (incident on the cavity, which corresponds to 68 W of peak drive power coupled into the cavity). Here we examine the resonance behavior for drive amplifier powers that vary from 100 mW to 2 W (Fig. S13). At each power we adjust the polarization of the drive to align to a single polarization state of the cavity by minimizing additional resonances. The output of the cavity is observed by detecting it on a photodiode after filtering out any spectral content outside of the central 20-GHz drive band with a fiber Bragg grating filter. The peak of the experimental resonance is shifted to match the peak from the equivalent numerical sweep. The numerical sweeps are obtained with noise-seeded simulations in which the detuning is varied after every round trip at a rate determined by the experimental sweep time.
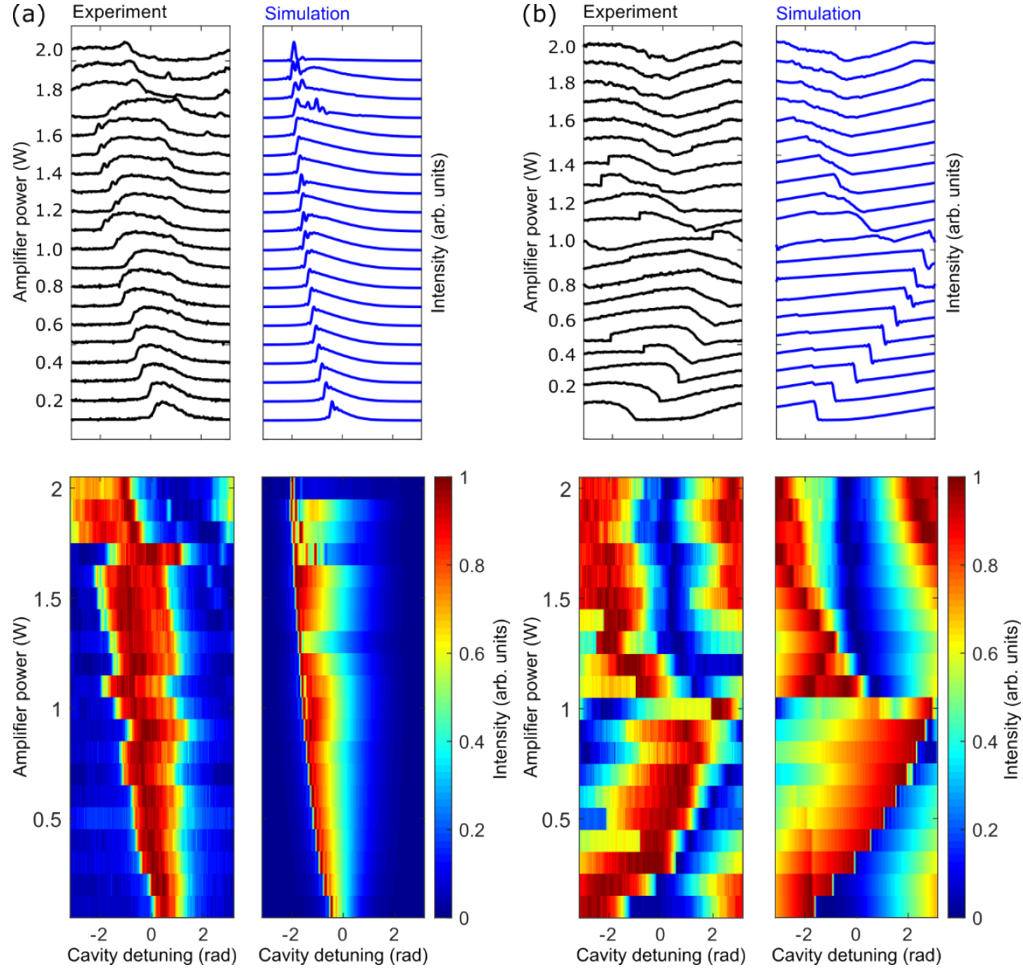
Fig. S13. Cavity resonance measurements and corresponding simulations. (Top) Experimental (black) and simulated (blue) intra-cavity continuous wave power as a function of the drive frequency detuning and average power (a) from negative to positive and (b) from positive to negative detuning. (Bottom) Color map representation of the same results. The resonance contains global information about the complex nonlinear system. Hysteresis is observed as a function of sweep direction.

Given the triangle wave used to drive the experimental frequency sweep, the resonance is swept from positive to negative detunings as well as from negative to positive detunings. With increasing detunings (Fig. S13(a)), the resonance peaks become broader with higher drive power. They are also shifted to negative detuning values. With decreasing detunings (Fig. S13(b)), the resonance behaves differently and is no longer around zero detuning at low power. The resonance is also broader and exhibits more structure. The qualitative agreement with experiment is in general good. There are also features that do not agree due to the complexity of this system. For example, there is some disagreement at higher drive powers in Fig. S13(a). Also, the step-like structures are inconsistent at around 1.1-W amplifier drive power in Fig. S13(b). There are several plausible explanations for these discrepancies related to environmental perturbations, polarization dynamics, pulse pumping dynamics, and the sensitive dependence on initial conditions. Since the cavity resonances are not actively stabilized, environmental thermal and acoustic perturbations will distort the resonance

observed. Any coupling between orthogonal polarization states in the cavity will produce additional resonances within this sweep range. In addition, dynamics resulting from the other polarization state can strongly affect the overall nonlinear dynamics and consequently the shape of the resonance. The present simulation neglects the polarization dynamics and assumes a single polarization state. Experimentally, the cavity is driven by a 10-ns drive pulse.

In the numerical simulations a continuous-wave drive is assumed because the drive pulse is much longer than the simulated temporal window. However, even a slight change in the drive magnitude as a function of time can lead to noticeable effects in the nonlinear dynamics of the system which would translate to changes in the resonance features. Finally, as emphasized in Supplementary Document Sections 4 and 6, the numerical simulations are complicated and feature multiple stable states, small basins of attraction, and a sensitive dependence on initial conditions. These complexities are all expected to be encountered when continuously traversing all of the different values of detuning. Many different classes of solutions, including dark solitons, switching waves, Turing patterns and chirped pulses can exist simultaneously within the same parameter space. In addition, each of these solutions can be obtained with different initial conditions, whereas in the simulation of the sweep, only one initial condition is chosen. We apply random intensity waveforms for the starting initial condition and by varying the detuning seed the next solution with the waveform that is obtained from the previous detuning. However, in practice, any small perturbations in the system will lead to different nonlinear pathways. In other words, sweeping over the parameters of a system sensitive to initial conditions further enhances this sensitivity, which complicates the analysis. Overall, it is remarkable to obtain qualitative agreement for resonances obtained from this highly nonlinear and complex system. Closer agreement may be obtained with a more complicated model that addresses the challenges summarized here.

15. Analysis of the intensity autocorrelations

For a collinear two-photon intensity autocorrelation the ratio of the detected signal peak to the background is dependent on the pulses as well as the residual continuous-wave background. Without the continuous-wave background, this peak-to-background autocorrelation ratio is 3 to 1 (this is the case for the pulses output from mode-locked lasers, for example). However, as the continuous-wave background increases, this ratio reduces. We illustrate this effect numerically with a Gaussian pulse on a continuous-wave background with a variable ratio of the relative amplitude of these two contributions (Fig. S14). We find that the autocorrelation contrast noticeably decreases when the amplitude of background to pulse peak approaches 0.5. In contrast, the ratio increases if there are more pulses in the cavity because the ratio of pulses to total background increases. It also increases when the chirped pulses compress because the pulse peak power increases. The autocorrelation background therefore conveys useful information about the chirp and pulse compression. In addition to the pulse duration (Fig. 3(f)) the autocorrelation background is also minimized when the pulse is dechirped (Fig. S14(d)). For comparison with numerical simulations, several assumptions are needed. The numerical temporal window is sampled over 100 ps to minimize computation time. Therefore, the background is extrapolated up to the full 10-ns duration of the drive pulse. After leaving the cavity, the background is filtered with a fiber-Bragg grating and then amplified with an Erbium-doped fiber amplifier before autocorrelation measurements. We find agreement with the experimental results with a net 15-dB attenuation of the background after these elements (Fig.

S14(e)). In summary, the autocorrelation ratio contains additional information regarding the complex waveform output from driven resonators.
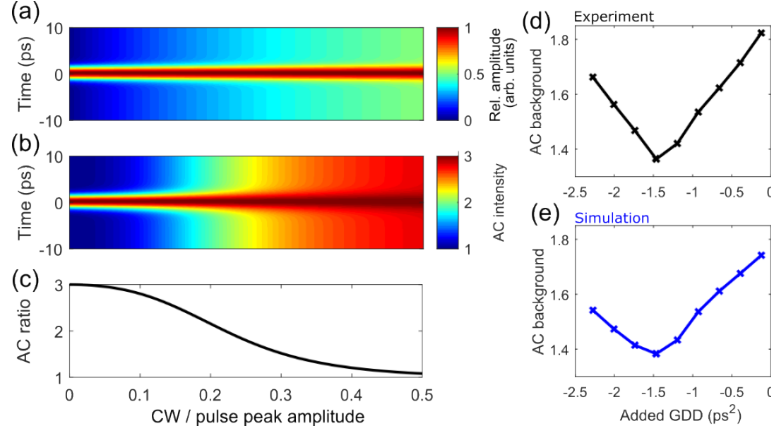

Fig. S14. Simulated autocorrelation of a pulse with a continuous background and comparison with experiment. (a) Pulse intensity profile, (b) autocorrelation profile and (c) autocorrelation ratio with the ratio of continuous-wave amplitude to the peak pulse amplitude of the waveform varying along the horizontal axis. (d) Experimental and (e) simulated autocorrelation ratio of the chirped dissipative solitons as a function of the GDD from the grating pair compressor with a minimum corresponding to the fully dechirped pulse.

16. Relationship between chirped dissipative solitons and other normal dispersion waveforms

In normal dispersion resonators, researchers have examined dark pulses [6-8] bright pulses [6], switching waves [9], platicons [10,11], and travelling front solutions [9]. Moreover, these solutions have been shown to be closely related to each other [9,10]. Here we explore the relationship between the chirped pulse solutions and previous solutions in the normal dispersion regime. Optical fibers are a nearly ideal waveguide for studying pulse propagation and so non-ideal effects, such as nonlocal coupling and higher-order group velocity dispersion are neglected. We examine and reproduce a subset of the solutions from Ref. [12] based on the Lugiato Lefever equation (LLE), to facilitate the comparison between different solutions. Numerically simulated solutions of the LLE (without a filter) are plotted in parameter space with respect to the analytical solutions for the continuous-wave solutions. The continuous-wave solutions are given by

$$D_0^{\pm}(\delta_{n0}) = \frac{1}{3}\left(-2\delta_{n0} \mp \sqrt{\delta_{n0}^2 - 3}\right)\left[1 + \frac{1}{9}\left(\sqrt{\delta_{n0}^2 - 3} \mp \delta_{n0}\right)^2\right],$$

where D_0^{+-} is the normalized drive power coefficient and δ_n0 is the normalized detuning coefficient. These expressions for the drive power are plotted as a function of detuning in green in Fig. S15. For reference, the critical value of the equilibria of the electric field squared, $\beta = D_0(\delta_{n0}) = 1 + (1 - \delta_{n0})^2$, is plotted as a dashed line [12]. We additionally reproduce the dark pulse solutions from Ref. [12] over a well-defined line in the detuning vs. drive parameter space. At low drive powers, dark solitons are observed. At higher drive powers the solutions develop a more complex structure. At higher drive powers the solutions become unstable and

the location of this boundary agrees well with the results in Ref. [12]. By introducing a spectral filter, even one with a broad 20-nm bandwidth, the location of the solutions within the parameter space shifts and the character of the solutions begin to change.
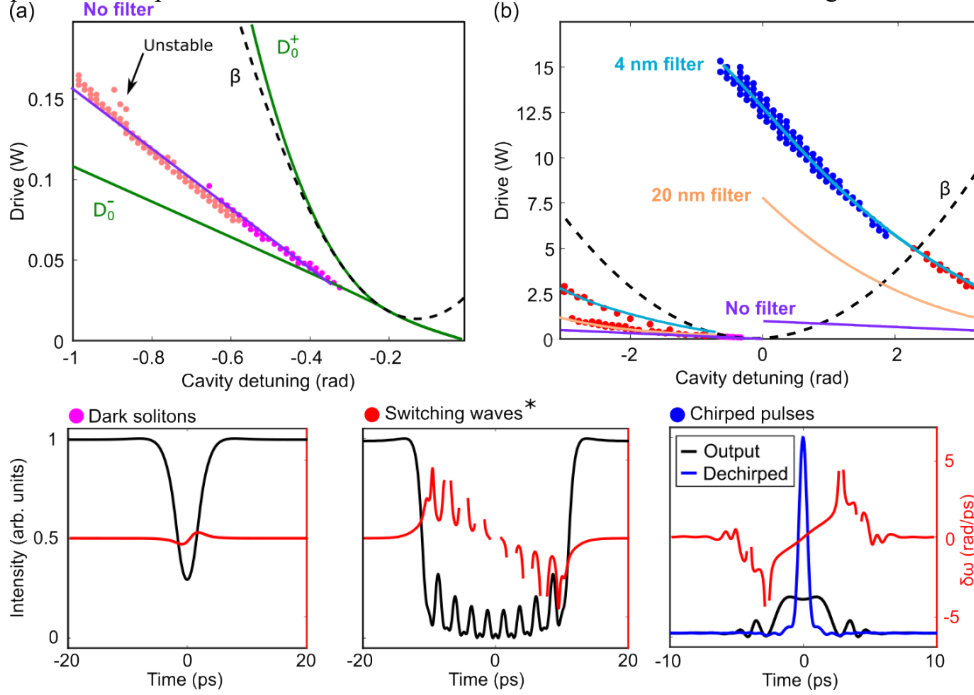

Fig. S15. Relation in parameter space between solutions in normal dispersion cavities. (a) Dark solitons in a normal-dispersion cavity without a spectral filter just above the analytically calculated lower branch D_0^- in excellent agreement with Ref. [12]. For drive powers > 0.1 W, solitons become unstable and do not converge. (b) With a 20-nm Gaussian spectral filter, dark solitons are found at low drive powers and complex dark solitons at higher drive powers. For powers >0.5 W, dark solitons appear as switching-waves. Switching waves evolve to chirped pulses featuring a decreasing peak duration and an increasing spectral bandwidth with narrower spectral filtering (light blue). Solid lines represent phenomenological fits to guide the reader. *These solutions have been referred to as switching waves, interlocking front solutions, or long complex dark pulses. Discontinuities in the instantaneous frequency $\delta\omega$ when the amplitude (intensity) approaches zero and the phase is not well defined are omitted.

The more complex dark solitons become stable and can exist with ten times higher drive powers (Fig. S15(b)). Moreover, the distinction between dark solitons, platicons, and switching waves begins to become less clear. In comparison to chirped solitons, these solutions do not have a quadratic spectral phase (or chirp) and their 3-dB bandwidth is narrow. If the bandwidth of the spectral filter is narrow enough (e.g. 4-6 nm as described in Supplementary Document, Section 7) and the drive power is sufficient, the bandwidth increases, the pulse duration decreases, and pulses with a well-defined chirp can form (Fig. S15(b)). Given the close relation in parameter space and the continuous evolution from dark solitons to chirped pulses, it is clear that the chirped pulses are related to the other solutions in normal dispersion resonators. Pulse formation in the normal dispersion cavities has been described as the result of interlocking switching-waves or front solutions [9]. Interestingly, the chirped pulse solutions in mode-locked lasers can also be described as the interlocking of traveling front solutions. Chirped-pulse mode-locked lasers are well described by the cubic quintic Ginzburg Landau equation which is known to possess chirped pulse solitons described in this way [13]. While this

relationship is suggestive, a thorough theoretical analysis will be needed to fully describe chirped dissipative solitons in passive cavities. Moreover, the complete set of solutions and dynamics for normal dispersion resonators with a filter is highly nontrivial (e.g. see Fig. 1 and Fig. S3). For example, in addition to the branch of solutions examined in Fig. 2, dark solitons, switching waves, and other solutions are also stable in completely different parameter regimes (Fig. 1 and Fig. S3). A comprehensive theoretical investigation for all of these nontrivial solutions will be important for future devices based on this novel filtered resonator design.

17. Comparison of chirped solitons to solitons in anomalous-dispersion cavities
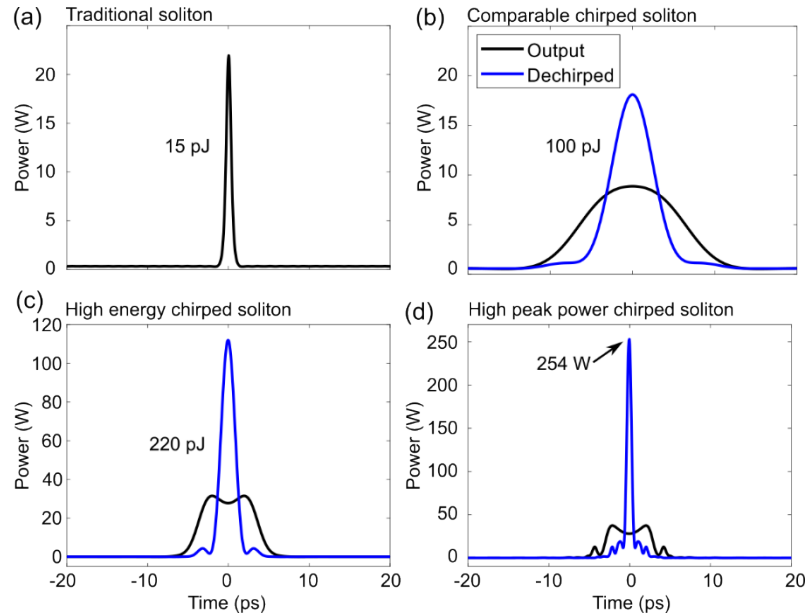

Fig. S16. Chirped dissipative soliton energy and peak power in comparison to traditional solitons. Stable soliton solution from numerical simulations of an (a) all-anomalous dispersion cavity without a filter and an (b) all-normal dispersion cavity with a 1-nm filter. The chirped-pulse soliton has around seven times higher pulse energy than the traditional soliton with the same drive power and magnitude of dispersion. (c) At higher drive powers, chirped dissipative solitons can support another two times higher energy than the traditional soliton. (d) High peak powers can be achieved after dechirping chirped dissipative solitons obtained with a spectral filter with a larger 6-nm bandwidth.

In mode-locked lasers, chirped solitons stabilize high pulse energies. In general, when the pulse is chirped, its peak power remains low, which reduces the destabilizing effects of nonlinearity. In normal dispersion resonators, chirped pulse mode-locked lasers have enabled pulse energies that are as much as two orders of magnitude larger than what can be achieved with traditional solitons [14-16]. Numerical simulations can help determine the relative energy of chirped-pulse solitons in passive resonators. We begin with the chirped-soliton resonator parameters for a 52.5-m normal dispersion fiber and a 4-nm bandwidth spectral filter. To examine comparable traditional solitons, we change the sign of the dispersion and remove the spectral filter. We find stable solitons over a well-defined region of drive powers and detuning values. As the drive power increases, the continuous-wave-background, and consequently the

solitons, begin to destabilize. We select the soliton that is noise-free and stable with the largest drive power as the high-performance representative for traditional solitons. The energy of the resultant pulse corresponds to 15 pJ inside the resonator with an intra-cavity drive power of 0.3 W and a detuning of -1.34 radians (Fig. S16(a)). In the normal dispersion cavity, chirped pulses exist over a wide range of drive powers and detuning values. However, the chirped pulses have a drive power threshold below which chirped pulses are not stable. For the 4-nm filter, chirped pulses are not stable at the 0.3-W drive power of the noise-free, stable traditional soliton. However, with a narrower 1-nm spectral filter, it is possible to stabilize chirped pulses with only 0.3-W of drive power. The resultant chirped pulses have pulse energies of 100 pJ, or about seven times more energy than the solitons (Fig. S16(b)). This result suggests that chirped pulses also carry a significant energy benefit in Kerr resonator systems.

In the previous result, the chirped-pulse drive power was constrained for direct comparison between the two types of solitons. However, higher energies may be possible for the chirped pulses with higher drive powers. To investigate, simulations are run for all possible drive detuning values as well as for much larger drive powers. Stable solutions are found for powers as much as fifty times higher than for the comparable anomalous dispersion cavity. The chirped-pulse energy is found to increase with increasing drive power. The bandwidth also increases with the drive power. Clean, noise-free pulses with energies of at least 220 pJ are observed in this cavity (Fig. S16(c)). This corresponds to more than ten times the energy of traditional solitons. However, the bandwidth of this chirped pulse is narrower than that of the soliton. By increasing the spectral filter, the bandwidth can be increase. For example, with a 6-nm spectral filter, we observe stable chirped pulses with a peak power enhancement that is greater than ten compared to traditional solitons (Fig. S16(d)). Numerical simulations therefore strongly suggest that much higher pulse energies and peak powers are achievable with chirped solitons than with the traditional solitons. Higher energy pulses for frequency combs corresponds to a higher power per comb line, which is an important performance parameter.

References

1. Chembo, Y. K. and Menyuk, C. R. Spatiotemporal Lugiato-Lefever formalism for Kerr-comb generation in whispering-gallery-mode resonators. Phys. Rev. A 87, 053852 (2013).
2. Anderson, M., Wang, Y., Leo, F., Coen, S., Erkintalo, M. and Murdoch, S. G. Coexistence of multiple nonlinear states in a tristable passive kerr resonator. Phys. Rev. X 7, 1–14 (2017).
3. Renninger, W. H. and Rakich, P. T. Closed-form solutions and scaling laws for Kerr frequency combs. Sci. Rep. 6, 24742 (2016).
4. Cundiff, S. T., Soto-Crespo, J. M. and Akhmediev, N. Experimental evidence for soliton explosions. Phys. Rev. Lett. 88, 739031–739034 (2002).
5. Chang, W., Ankiewicz, A., Soto-Crespo, J. M. and Akhmediev, N. Dissipative soliton resonances. Phys. Rev. A 78, 23830 (2008).
6. Xue, X., Xuan, Y., Wang, P. H., Liu, Y., Leaird, D. E., Qi, M. and Weiner, A. M. Normal-dispersion microcombs enabled by controllable mode interactions. Laser Photonics Rev. 9, L23–L28 (2015).
7. Jang, J. K., Erkintalo, M., Schroder, J., Eggleton, B. J., Murdoch, S. G. and Coen, S. All-optical buffer based on temporal cavity solitons operating at 10 Gb/s. Opt. Lett. 41, 4526–4529 (2016).
8. Liang, W., Savchenkov, A. A., Ilchenko, V. S., Eliyahu, D., Seidel, D., Matsko, A. B. and Maleki, L. Generation of a coherent near-infrared Kerr frequency comb in a monolithic microresonator with normal GVD. 39, 2920–2923 (2014).
9. Parra-Rivas, P., Gomila, D., Knobloch, E., Coen, S. and Gelens, L. Origin and stability of dark pulse Kerr combs in normal dispersion resonators. Opt. Lett. 41, 2402–2405 (2016).
10. Lobanov, V. E., Lihachev, G., Kippenberg, T. J. and Gorodetsky, M. L. Frequency combs and platicons in optical microresonators with normal GVD. Opt. Express 23, 7713–7721 (2015).
11. Fülöp, A., Mazur, M., Lorences-Riesgo, A., Eriksson, T. A., Wang, P.-H., Xuan, Y., Leaird, D. E., Qi, M., Andrekson, P. A., Weiner, A. M. and Torres-Company, V. Long-haul coherent communications using microresonator-based frequency combs. Opt. Express 25, 26678 (2017).

12. Godey, C., Balakireva, I. V., Coillet, A. and Chembo, Y. K. Stability analysis of the spatiotemporal Lugiato-Lefever model for Kerr optical frequency combs in the anomalous and normal dispersion regimes. Phys. Rev. A 89, 063814 (2014).

13. Soto-Crespo, J. M., Akhmediev, N. N., Afanasjev, V. V and Wabnitz, S. Pulse solutions of the cubic-quintic complex Ginzburg-Landau equation in the case of normal dispersion. Phys. Rev. E 55, 4783–4796 (1997).

14. Renninger, W. H., Chong, A. and Wise, F. W. Pulse shaping and evolution in normal-dispersion mode-locked fiber lasers. IEEE J. Sel. Top. Quantum Electron. 18, (2012).

15. Renninger, W. H., Chong, A. and Wise, F. W. Giant-chirp oscillators for short-pulse fiber amplifiers. Opt. Lett. 33, 3025–3027 (2008).

16. Chong, A., Renninger, W. H. and Wise, F. W. All-normal-dispersion femtosecond fiber laser with pulse energy above 20nJ. Opt. Lett. 32, 2408–2410 (2007).